CORRESPONDENCE

Experimental study on the effect of loading rate on the strain energy accumulation and release during the weakening process of circular-tunnel

Xun You · Yunmin Wang · Xiangxin Liu · Kui Zhao · Zhengnan Zhang

Abstract The weakening of circular tunnels is a global problem that has not been resolved satisfactorily. In the tunnelling process, surrounding rock of circular-tunnel performs a process of "excavating→weakening→continuous excavating→weakening strengthens". Different rates of excavation affect the stress adjustment of the surrounding rock, and also have an impact on the weakening of a circular-tunnel. An instability failure test was conducted on a circular-tunnel with varying vertical loading rates. The loading rate was utilized as a representative measure for the excavation rate on the *site*. The results showed that the weakening process of a circular-tunnel can be divided into four distinct phases, hydrostatic pressure ($E1$), particle ejection ($E2$), flake stripping ($E3$), and instability ($E4$). The ordering of these phases is $E3 > E4 > E1 > E2$. In the weakening process of a circular-tunnel, the root cause is the original stress level, while the essential factor is the engineering disturbance. A faster vertical loading rate leads to greater stress adjustment, higher strain energy accumulation, and an increased probability of circular-tunnel instability. The presence of a quiet period of AE events in the middle and later phases of flake stripping is a precursory characteristic of circular-tunnel instability. This study has both theoretical and practical significance in terms of revealing the mechanism of circular-tunnel instability and achieving a reasonable arrangement of the circular-tunnel support process.

X. You · Y. Wang · K. Zhao · Z. Zhang
School of Resource and Environmental Engineering, Ganzhou, China

X. You
Baowu Resources Corporation Limited, Shanghai 200126, China

Y. Wang
State Key Laboratory of Safety and Health for Metal Mines, Maanshan 243000, China

X. Liu (✉)
School of Civil and Surveying and Mapping Engineering, Jiangxi University of Science and Technology, Ganzhou 341000, China
e-mail: LiuXX@jxust.edu.cn

Article Highlights

(1) The intensity of circular tunnel fracturing is found to increase with higher vertical loading rates and greater strain energy migration. Specifically, the hydrostatic pressure phase is identified as the phase associated with the largest amount of strain energy.

(2) Strain energy migration is identified as a useful indicator of the weakening process in a circular tunnel. It provides valuable information about the redistribution and accumulation of energy within the tunnel structure, which can help in understanding the progression of tunnel instability.

Abbreviations

E1	Hydrostatic pressure phase
E2	Particle ejection phase
E3	Flake stripping phase
E4	Instability phase
$\theta\prime$	A key parameter to distinguish shear and tensile cracks
θ	The angle between RA' and AF'

1 Introduction

The instability mechanisms of rockmass, particularly in tunnels, pose significant challenges in underground engineering worldwide (Hyun-Ik et al. 2009; Gong et al. 2019, 2023). Understanding the variation characteristics of strain energy is crucial for gaining quantitative insights into the precursors of tunnel instability (Liu et al. 2014; Si et al. 2022; Zhang et al. 2023). It is important to clarify the features of energy input, accumulation, dissipation, and release during the weakening process for practical applications and theoretical significance (Xie et al. 2008; Zhang et al., 2015; Hou et al. 2016; Gao et al. 2020).

The accumulation and release of strain energy have become increasingly important in understanding rock failure processes. Researchers have studied the energy evolution of coal in rock masses surrounding boreholes and utilized the dissipated energy release for structure monitoring, employing the energy principle (Jing and Zhang 2022). In water-saturated conditions, rocks typically exhibit reduced ability to absorb strain energy, which in turn promotes energy dissipation behavior (Zhang et al. 2015; Niu et al. 2018). The fracture mode of rock can transition from shear to tensile, and the ratio of energy transformation before and after the peak is positively correlated with unloading rates (Huang and Li 2014). The criterion established by Feng et al. (2024) provided a new understanding of the effect of strain rate on dynamic rock strength (Feng et al. 2024). In true triaxial rock failure tests, researchers have discovered an energy evolution law indicating that the energy storage limits and elastic energy density of rock increase with the rise of the second and third principal stresses. The third principal stress promotes rock energy dissipation, while the second principal stress inhibits it (Zhang et al. 2019a, 2019b). Microseismic monitoring, combined with the moment tensor inversion method, has proven to be a valuable approach for understanding rockbursts in tunnels. Abundant data obtained from microseismic monitoring allows for the analysis of statistical parameters and waveform characteristics, which can serve as early warning indicators of rockbursts (Liang et al. 2020; Xue et al. 2020). Moreover, the combination of microseismic monitoring and moment tensor inversion contributes to clarifying the mechanical mechanisms controlling the failure modes of surrounding rock and enables a reasonable and accurate identification of the failure mechanism of rock masses (Zhao et al. 2024).

Acoustic emission (AE) features play a crucial role in monitoring and understanding rock failure processes. Various studies have highlighted the significance of AE monitoring in revealing the characteristics of rock failure (Lavrov 2003; Ohtsu et al. 2007; Zhai et al. 2022; Dong et al. 2023). The AE energy index is particularly valuable as it represents the energy dissipation during the evolution of rock fracturing (Meng et al. 2016; Liu et al. 2019; Wang et al. 2023). Monitoring AE information provides insights into the coupling effect between initial damage and mechanical loading damage. It can be divided into several stages based on AE energy, including the initial low-level stage, the relatively stable stage before the peak, the peak burst stage, the dense stage after the peak, and the relatively stable stage of residual intensity (Zhao et al. 2023). Additionally, the average frequency centroid of AEs has been found to reveal precursory characteristics for critical failures in red sandstone with different water contents (Zhao et al. 2021a, b).

In this paper, the focus is on examining the influence of loading rates on the energy change during the circular-tunnel weakening process. The researchers investigate the accumulation and release features of strain energy to understand the mechanism of circular-tunnel instability. By considering three different vertical loading rates, they analyze the formation mechanism of circular-tunnel instability from the perspective of strain energy movements.

2 Basic theories

The equation of energy balance during the deformation and failure of rock can be expressed as,

$$E_i = E_k + E_\xi + E_a = E_k + E_\xi + E_s + E_h$$

where, E_i is the total input energy. E_k is the kinetic energy. E_ξ is the viscous damping dissipates energy. E_a is the absorb energy. E_s is the elastic strain energy. E_h is the hysteresis dissipates energy. $E_a = E_s + E_h$.

In the closed system of "tunnel-surrounding rock", when the released energy is greater than the sum of the various energies consumed, it is possible to lose stability, and its mathematical expression is as,

$$\left[\alpha \bullet \left(\frac{dW_E}{dt} \right) + \beta \bullet \left(\frac{dW_S}{dt} \right) \right] > \left(\frac{dW_D}{dt} \right) \quad (1)$$

where W_E is the deformation energy stored by the closed system. α is the energy release coefficient of the closed system. W_S is the strain energy accumulated by tunnel excavation disturbance. β is the corresponding strain energy accumulation coefficient under disturbance. W_D is the energy dissipation of tunnel failure.

In this study, the stress boundary conditions are set as, the maximum principal stress σ_1 is the axial stress, and the intermediate principal stress σ_2 is the horizontal stress. For the force at any place in the tunnel model, it is represented by a 2×2 stress matrix, namely as,

$$d\sigma_i = \begin{bmatrix} d\sigma_{1i} & 0 \\ 0 & d\sigma_{2i} \end{bmatrix} \quad (2)$$

The deformation generated by stress at any point in the tunnel model can also be represented by a 2×2 strain tensor matrix, namely as,

$$d\varepsilon_i = \begin{bmatrix} d\varepsilon_{1i} & 0 \\ 0 & d\varepsilon_{2i} \end{bmatrix} \quad (3)$$

Stress is divided into two parts, one part represents the overall change of volume, namely the effect of normal stress. The other part represents the change of microelement shape, which is the effect of deviatoric stress. The change of microelement shape represents the plastic deformation of tunnel and produce fracture effect. Therefore, deviatoric stress can be solved directly as follows:

$$d\sigma_{ij} = d\sigma_{1i} - d\sigma_{2i} \quad (4)$$

The strain tensor of any points in the stressed body can be decomposed into spherical strain tensor and partial strain tensor. The stress component of the point can be solved as follows:

$$d\varepsilon_{ij} = \frac{1}{2} \times (d\varepsilon_{1i} + d\varepsilon_{2i}) \quad (5)$$

Deformation and fracture of rock are primarily attributed to deviatoric stress. The deviatoric strain is a physical quantity that characterizes the deformation response of rock mass under deviatoric stress. The direction of these two quantities is identical, and their product represents the work performed by deviatoric stress. Consequently, it is possible to determine the amount of energy input during the stability weakening of a tunnel model by the following formula:

$$\omega_{ij} = d\sigma_{ij} \times d\varepsilon_{ij} \quad (6)$$

As per Eq. 6, the energy input during the weakening of circular-tunnel stability mainly comprises the energy stored within the rock mass before excavation and the energy increment resulting from the disturbance caused by excavation. On the other hand, the energy loss is primarily associated with the energy dissipated during the deformation and failure of the circular-tunnel model. Thus, it is plausible to evaluate the weakening process of the circular-tunnel stability by comparing the energy input from strain with the dissipated energy.

3 Circular-tunnel instable failure test

3.1 Circular-tunnel model preparation

In this study, underground engineering granite was selected, which predominantly consists of minerals such as quartz, mica, hornblende, and plagioclase. Due to variations in the strength of these minerals, the heterogeneous nature of crystal bonding between particles, and the presence of natural defects in the structure of these minerals, the granite exhibits sensitivity to stress and holds immense research value.

To comply with the recommendations of *ISRM* and meet the experimental requirements, the

Fig. 1 Circular-tunnel model
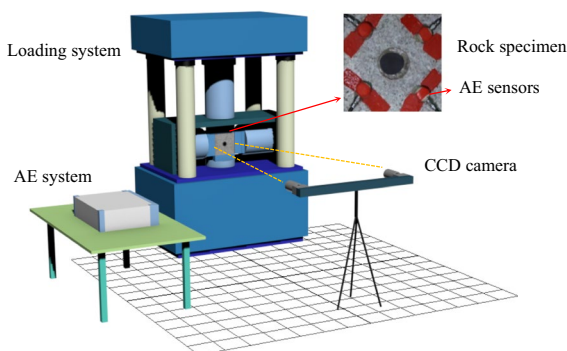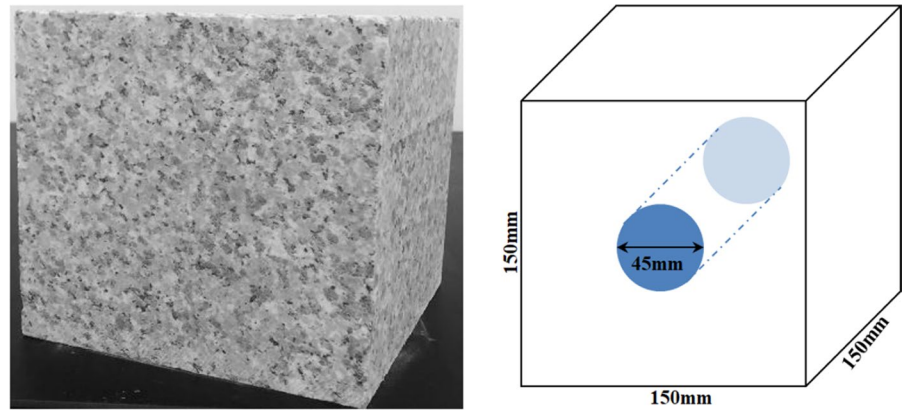
Fig. 2 Schematic diagram of the experimental system

granite sample was processed using *ISRM*-approved methods to form a standardized cube measuring $150 \times 150 \times 150$ mm³. As shown in Fig. 1, a circular through hole with a diameter of 45 mm was drilled at the center of the specimen. Vertical loading rates of 0.3 mm/min, 0.4 mm/min, and 0.5 mm/min were employed, and four data points were collected at each rate.

3.2 Test equipment setting

The experimental system is mainly composed of loading device, AE system and CCD camera, as shown in Fig. 2. The setup of the laboratory equipment should be consistent to guarantee the conformity of experiment data of different rock specimens (Ishida et al. 2017). The basic performance parameters of each equipments are as follows:

(1) Loading system: RLW-3000 servo pressure testing machine is used in this study, the maximum axial pressure is up to 3000 kN, the maximum lateral pressure reached 1000 kN. The control accuracy on two loading ends is less than $\pm 1\%$.

(2) AE system: The fracturing characteristics of weakening process of circular-tunnel stability were recorded by eight AE detectors (PCI-2, Physical Acoustics Corporation, United States). Multiple AE parameters, such as waveforms, hits, ring-down counts, and amplitudes, are collected by eight AE sensors.

(3) CCD camera: The model of CCD camera is used Pike F-421 (Germany). The spatial resolution of CCD camera is set as 640 pixels $\times$ 512 pixels. The sampling rate is set up to 80P/s, respectively.

4 Results and discussions

4.1 Experimental results

4.1.1 Phase division of stability weakening of circular-tunnel model

As depicted in Fig. 3, the evolution of instability in the circular-tunnel occurs in four distinct phases: the hydrostatic pressure phase, the particle ejection phase, the flake stripping phase, and the instability phase. These phases characterize the weakening process of the circular-tunnel model.

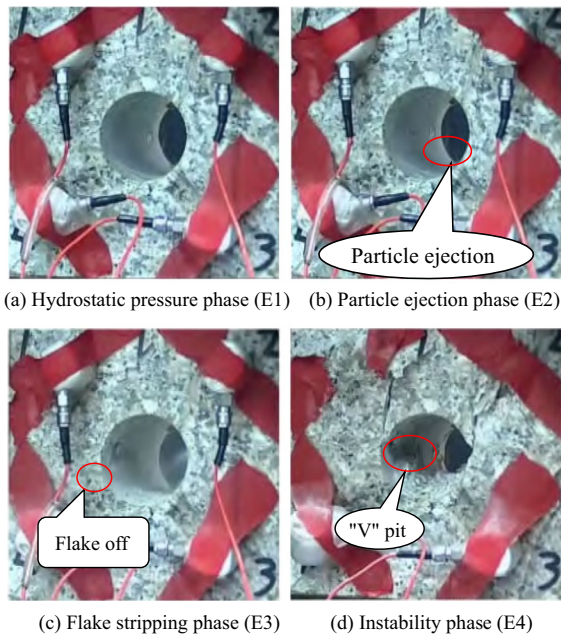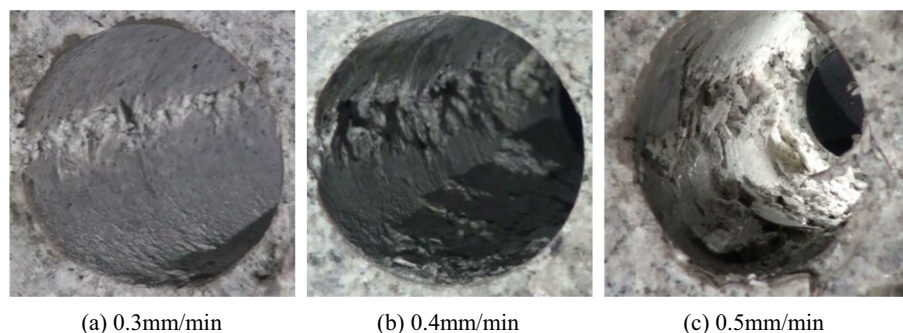(1) Hydrostatic pressure phase (E1, Fig. 3a): Due to the low stress levels, no obvious fracturing phe-

(a) Hydrostatic pressure phase (E1)   (b) Particle ejection phase (E2)

(c) Flake stripping phase (E3)   (d) Instability phase (E4)

Fig. 3 The photograph of the weakening process of circular-tunnel

nomenon was observed in the surrounding rock of the circular-tunnel.

(2) Particle ejection phase (E2, Fig. 3b): As the vertical stress increases to a certain degree, a small-scale particle ejection was observed at the lumbar line position of the surrounding rock.

(3) Flake stripping phase (E3, Fig. 3c): As the axial stress continues to increase, the cracking phenomena of the lumbar line position of the surrounding rock gradually expanded. Initially, small particle ejections developed into flake off and eventually progressed to particle mixing with continuous ejection.

(4) Instability phase (E4, Fig. 3d): As the axial stress further increases to a critical point, the surrounding rock experiences intense particle ejections. Large amounts of particles burst from the wall with great force, accompanied by a distinct crackling sound. The lumbar line exhibits a continuous "V" shaped explosion pit, and a significant amount of debris particles accumulates at the bottom of the circular-tunnel model.

4.1.2 The failure phenomena of circular-tunnel surrounding rock

Figure 4 demonstrates that as the loading rates increase, the failure phenomenon of the surrounding rock in the circular roadway becomes more severe and affects a larger area.

(1) 0.3 mm/min (Fig. 4a): During the failure process of the surrounding rock in the circular roadway, the type of debris that is ejected typically consists of small particles or flakes. The sound of instability is relatively mild, resembling the sound of breaking twigs with occasional crackling noises. Initially, small particles are ejected, followed by the ejection of some small fragments. Finally, slight failure on the wall surface and a narrow instability pit may appear.

(2) 0.4 mm/min (Fig. 4b): The type of debris that is ejected during the failure process of the surrounding rock in the circular roadway includes not only flaky mixtures but also small particles. The sound of instability is dominated by a mild crackling sound. At the beginning of the failure process, small particles are ejected and flakes peel off and are ejected. Eventually, a large amount of rock powder

Fig. 4 The photograph of final instable of the circular-tunnel

(a) 0.3mm/min   (b) 0.4mm/min   (c) 0.5mm/min

is ejected as well. The final damage area is greater than 0.3 mm/min, and the resulting crater is deeper.

(3) 0.5 mm/min (Fig. 4c): The type of debris that is mainly ejected during the failure process of the surrounding rock in the circular roadway is tabular debris. The sound of instability is dominated by continuous crackling. The failure process is primarily characterized by lamellar peeling, with a small amount of particles being ejected and a large amount of rock powder being ejected as well. Eventually, the damage becomes severe, and the inner wall of the circular-tunnel suffers significant damage. An obvious "V" shaped explosion crater may form, and a large amount of suspended debris may remain on the section.

4.1.3 The crack type variation of surrounding rock during the weakening process

The type of crack that appears in the surrounding rock of the circular roadway is dependent on the stress conditions and closely linked to the release of strain energy. In this context, the relationship between the RA-AF and crack type can be identified. The RA-AF relationship can be calculated using various AE parameters such as rise time, amplitude, counts, and duration time as shown in Eq. 7 (Shiotani 2008).

$$\begin{cases} RA = \dfrac{RiseTime}{Amplitude} \\ AF = \dfrac{Counts}{DurationTime} \end{cases} \quad (7)$$

To classify the crack type, the vectors of [RA, AF] are populated for RA and AF, respectively, as shown in Eq. 7. The crack type is then divided into two modes: Mode I, which is a tensile crack characterized by high AF values and low RA values, and Mode II, which is a shear crack, characterized by low AF values and high RA values (Farhidzadeh et al. 2014). This division is illustrated in Fig. 5a.

Figure 5b shows a proportional distribution of the relative number of tensile and shear cracks. While this qualitative description provides valuable insights, in order to capture the quantitative features of tensile and shear cracks, some processing is required. This processing can be achieved using Eqs. 8 to 10. Normalization step are used to deal with AF and RA, and AF' and RA' is solved as follows,

$$\begin{cases} AF'_i = \dfrac{[AF_i - min(AF)]}{[max(AF) - min(AF)]}, i = 1 \dots \dots N \\ RA'_i = \dfrac{[RA_i - min(RA)]}{[max(RA) - min(RA)]}, i = 1 \dots \dots N \end{cases} \quad (8)$$

θ' is a key parameter to distinguish shear and tensile cracks (Fig. 5b). $\tan\theta$ is solved as follows,

$$\tan\theta' = \frac{AF'_i}{RA'_i} \quad (9)$$

$$\begin{cases} \tan\theta' > 1, tensile crack \\ \quad else, shear crack \end{cases} \quad (10)$$

Figures 6 and 7 are the energy and counts of tensile or shear cracks in different phases. The characteristics on each phase are as:

(1) Hydrostatic pressure phase (E1): As shown in Fig. 6 (E1), there are significantly more tensile cracks than shear cracks. At a loading rate

Fig. 5 Schematic diagram of crack classification. **a** Before normalization (Farhidzadeh et al. 2014); **b** after normalization)
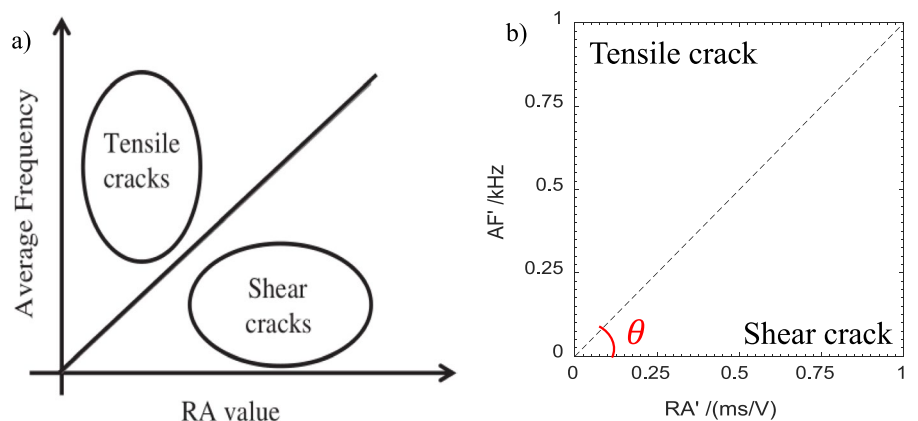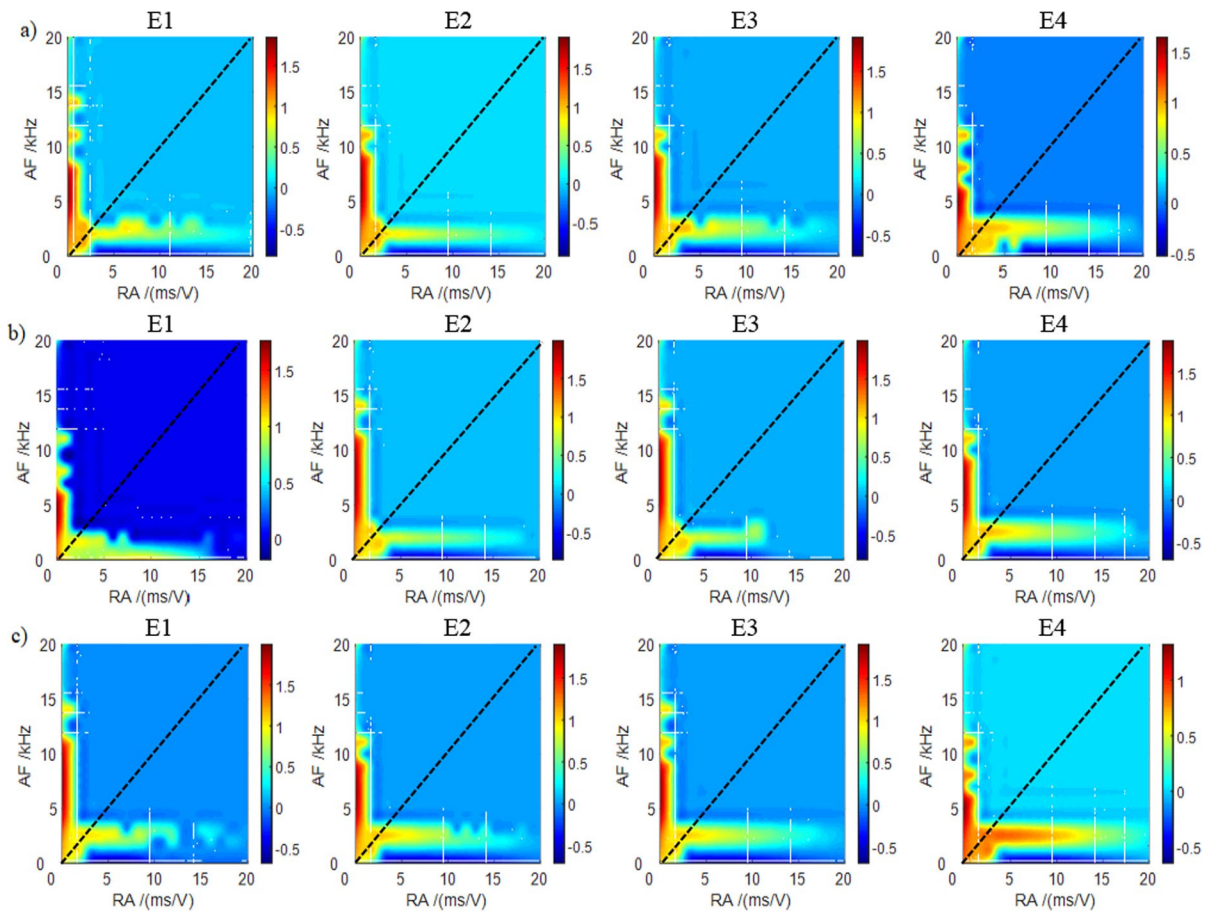
Fig. 6 The crack type in different phase by RA-AF's relationship. **a** 0.3 mm/min; **b** 0.4 mm/min; **c** 0.5 mm/min

of 0.4 mm/min, the energy index of both tensile and shear cracks reaches high counts, as shown in Fig. 6. Additionally, cracks are developed in areas of lower energy, as illustrated on the left side of Fig. 7. In this area, tensile crack makes up the largest proportion of all crack types, as seen on the right side of Fig. 7.

(2) Particle ejection phase (E2): At a loading rate of 0.3 mm/min, the energy index of both tensile and shear cracks is larger than in the E1 phase, as shown in Fig. 6. However, the number of shear cracks is significantly smaller than that of tensile cracks at loading rates of 0.4 mm/min and 0.5 mm/min. Moreover, the AE energy is lower in areas where cracks are developed, as illustrated on the left side of Fig. 7, and the AE counts are smaller compared to the E1 phase, as seen on the right side of Fig. 7.

(3) Flake stripping phase (E3): In shear fracturing events at lower loading rates of 0.3 mm/min and 0.4 mm/min, the energy index is associated with fewer numbers of cracks. However, at a loading rate of 0.5 mm/min, the energy index is high, resulting in large amounts of shear cracks, as shown in Fig. 6. In all situations, the AE energy of both tensile and shear cracks is lower in areas where cracks are developed, as illustrated on the left side of Fig. 7. Additionally, the counts of tensile cracks are larger than those of shear cracks, as seen on the right side of Fig. 7.
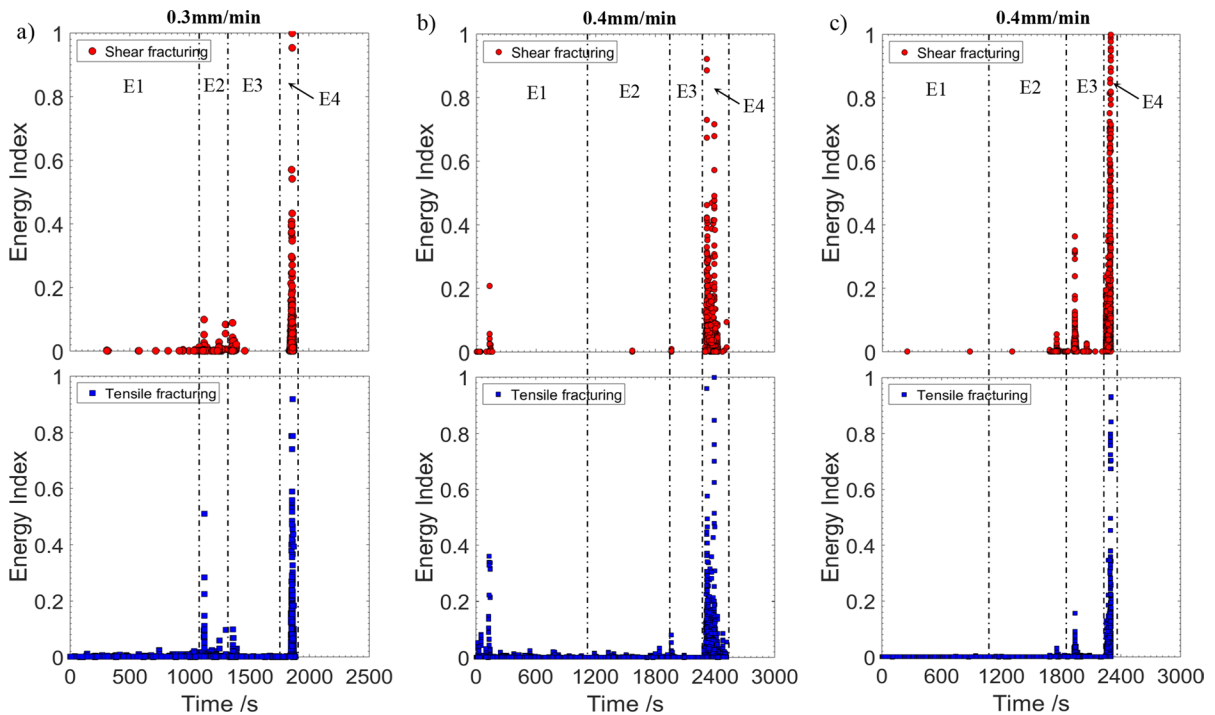
Fig. 7 The cracks distribution along rock fracturing process. **a** 0.3 mm/min; **b** 0.4 mm/min; **c** 0.5 mm/min

(4) Instability phase (E4): The energy index of both tensile and shear cracks reaches its highest value, as shown in Fig. 6. Additionally, the AE energy of shear cracks is higher than that of tensile cracks in areas where cracks are developed, as illustrated on the left side of Fig. 7. However, the counts of tensile cracks are larger than those of shear cracks, as seen on the right side of Fig. 7.

The ratio of shear crack is significantly lower than tensile in the previous three phases, there energy value also smaller than the final phase. Big energy events are happen in E4 phase. The maximum energy value is presented in the type of shear crack on both loading rates of 0.3 mm/min and 0.5 mm/min, the maximum energy value in 0.4 mm/min is tensile crack type. The strength criterion is also beneficial to measure the key failure information. Zhao et al. (2021a, b) developed a new calculation method based on two indices, compressive strength and tensile strength, and discovered that the accuracy of tensile strength test results is closely linked to the compression-tension ratio.

4.2 Strain energy accumulation and release of circular-tunnel weakening process

4.2.1 The features of strain energy accumulation

The number of strain energy accumulations during the weakening process of a circular tunnel is solved by Eq. (6). The curves of strain energy in each phase are shown in Fig. 8, while the curves of cumulative strain energy during the weakening process of the circular tunnel are illustrated in Fig. 9. The cumulative variation law of strain energy on hydrostatic pressure phase (E1), particle ejection phase (E2), flake stripping phase (E3), and instability phase (E4) are as follows:

(1) Hydrostatic pressure phase (E1): The energy accumulation values corresponding to the three loading rates are around 15 kJ, which suggests that they are not affected by the loading rate.
(2) Particle ejection phase (E2): The inner wall of the circular tunnel shows a small number of particle ejections, and the amount of strain energy input is at a low level, as shown in Fig. 8. From the
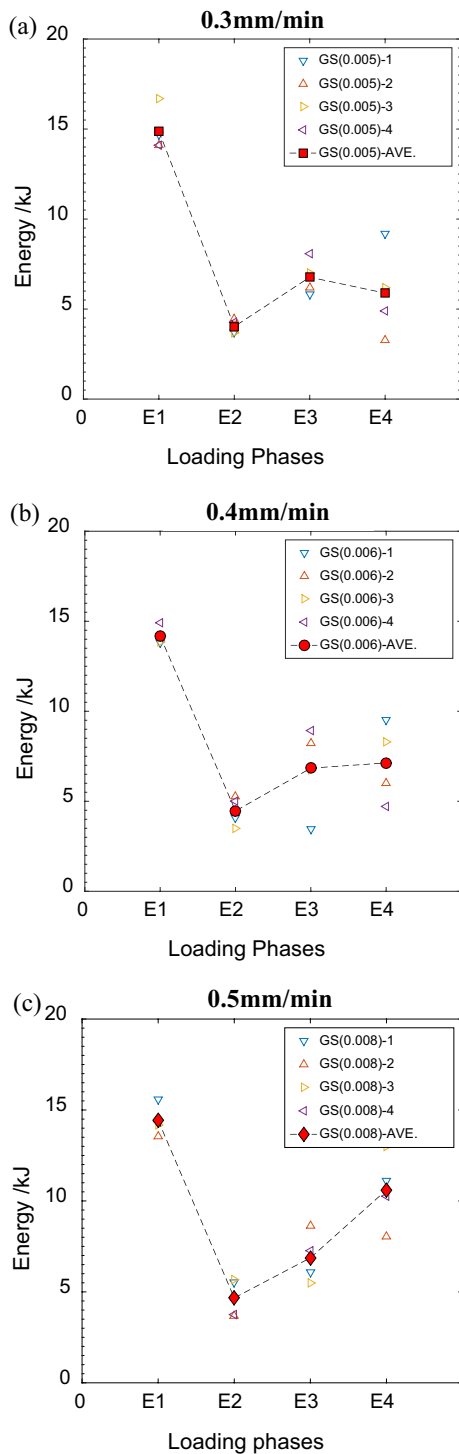
Fig. 8 The curves of strain energy on each phase during weakening process of circular-tunnel

hydrostatic pressure phase to the particle ejection phase, the cumulative strain energy in the loading rate of 0.5 mm/min is slightly higher compared to the other loading rates, as illustrated in Fig. 9.

(3) Flake stripping phase (E3): The strain energy in the E3 phase is significantly higher than that in the particle ejection phase (E2). Among the three loading rates, the loading rate of 0.5 mm/min has the largest increase in strain energy (as shown in Fig. 8) and the most significant increasing trend in cumulative strain energy during the weakening process of the circular tunnel (as shown in Fig. 9).

(4) Instability phase (E4): The strain energy dissipation in this phase is significantly higher compared to other phases, and the storage strain energy property in this phase is the weakest among all phases. In this phase, the strain energy values for the loading rates of 0.3 mm/min and 0.4 mm/min are slightly less than that in the flake stripping phase, while the strain energy value for the loading rate of 0.5 mm/min is significantly larger than that in the flake stripping phase (as shown in Fig. 8). Moreover, the growth rate of cumulative strain energy in the loading rate of 0.5 mm/min is the largest among all loading rates (as shown in Fig. 9).

The hydrostatic pressure phase (E1) has the largest amount of strain energy among all phases. This reflects that the depth of the underground structure to a certain extent determines the possibility of rock mass failure, i.e., the original stress level of the underground rock mass is the root cause of its failure. The cumulative strain energy variations exhibit a trend of growth (as shown in Fig. 10). The strain energy of the rock mass increases due to engineering disturbance, which is the cause of the failure of the rock mass.

4.2.2 The features of strain energy release

Previous studies have shown that there is a positive correlation between the amount of strain energy storage, the intensity of rock fracturing events, and the degree of strain energy dissipation (Huang and Li 2014; Zhang et al. 2019c). Acoustic Emission (AE) events represent the regularity of fracturing activity, while the cumulative AE energy is a feature of strain energy dissipation. Figure 10 illustrates the evolution

Fig. 9 The curves of cumulative strain energy on each phase ▶ during weakening process of circular-tunnel

of circular tunnel weakening as characterized by AE events and cumulative AE energy:

(1) Hydrostatic pressure phase (E1): AE cumulative energy exhibits low levels for all three loading rates. However, there are significant differences in AE events, with the most active AE event occurring at a loading rate of 0.3 mm/min, followed by 0.4 mm/min, and the weakest AE event occurring at 0.5 mm/min.

(2) Particle ejection phase (E2): The AE cumulative energy remains relatively low for all loading rates. There are also some differences in the performance of AE events, with the loading rates of 0.3 mm/min and 0.5 mm/min exhibiting more activity than in the previous phase, while the loading rate of 0.4 mm/min exhibits the same level of activity as in the previous phase.

(3) Flake stripping phase (E3): The AE cumulative energy for the loading rates of 0.3 mm/min and 0.5 mm/min exhibit a step-like growth pattern, while the growth pattern for the loading rate of 0.4 mm/min is not significant enough. In terms of AE events, all three loading rates show consistency and are weaker than in the previous phase.

(4) Instability phase (E4): All three loading rates exhibit a step-like jump in both AE events and cumulative energy over a short period of time. The loading rate of 0.5 mm/min exhibits slightly stronger AE events than the other two rates, and its corresponding AE cumulative energy is also greater than that of the other two rates.

4.3 Tunnel instable failure on *site*

Tunnel instable failure, while not leading to full collapse, is a type of localized fracturing event. The results of the tunnel model failure in this study exhibited localization characteristics, which were observed not only in laboratory-scale simulation experiments (Figs. 3c and d), but also at underground mine sites (Fig. 11). The "V" shape observed in the central section of the tunnel was found to be a typical feature of brittle failure, which was consistent across both laboratory-scale and mine site observations. However,
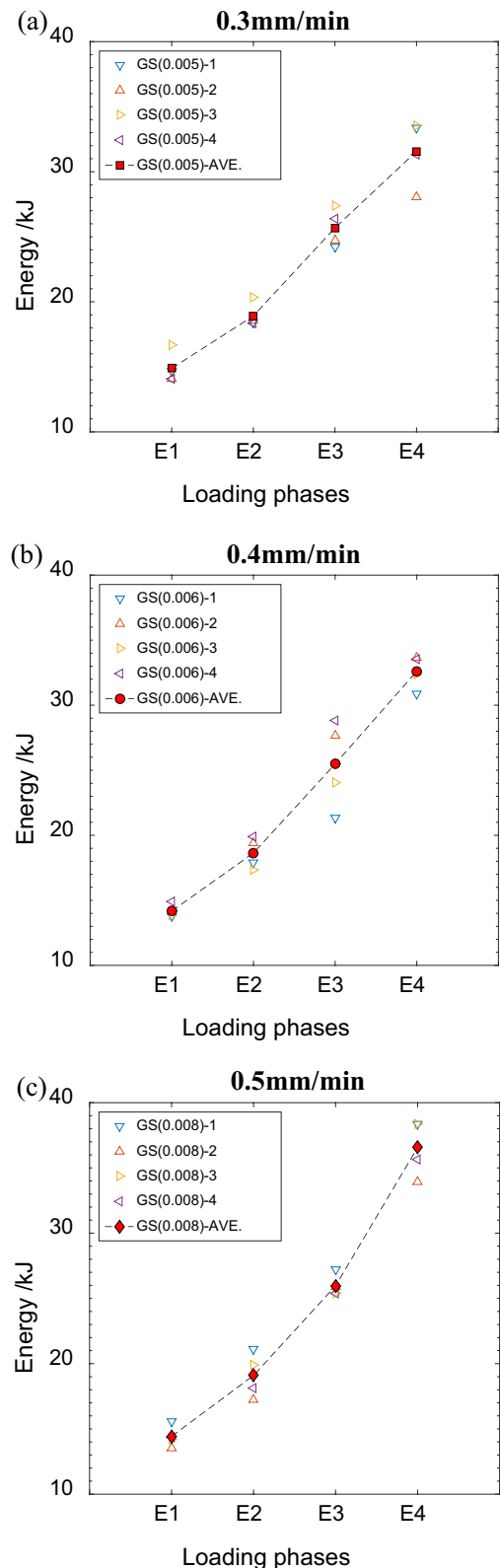
Fig. 10 the curves of AE event and AE cumulative energy ▶ during weakening process of circular-tunnel

the types, locations, and intensities of fracturing varied significantly among different tunnels. Relying solely on monitoring parameters is not sufficient to fully capture the weakening and instability features of tunnels.

Exploring the accumulation and release of strain energy is crucial for fully understanding the characteristics of circular-tunnel stability weakening. One phenomenon that deserves particular attention is the significant decrease in AE event activity during the middle and later stages of flake stripping, as shown in Fig. 11. This period of decreased AE activity is referred to as the "AE quiet period", and is considered to be a precursory feature of instability failure (Yin et al. 2009; Smittarello et al. 2022; Chen et al. 2023). Understanding this characteristic can provide valuable insights into tunnel stability and potential failure mechanisms.

5 Conclusions

(1) The process of weakening in circular tunnels exhibits distinct phase characteristics, including the hydrostatic pressure phase, particle ejection phase, flake stripping phase, and instability phase. As the vertical loading rates increase, the intensity of circular-tunnel fracturing begins to increase, as does the migration of strain energy.

(2) As the vertical loading rates increase, the damage to the rock specimens becomes more severe, making it increasingly difficult to adjust the strain energy. During the hydrostatic pressure phase, the strain energy reaches its maximum value, with the cumulative strain energy variations exhibiting a steady increasing trend.

(3) Strain energy migration is a valuable indicator of the evolution of circular-tunnel weakening. The AE quiet period observed during the middle and later phases of flake stripping is a particularly useful precursory feature of circular-tunnel instability failure. By tracking strain energy migration and monitoring AE event activity, it may be possible to predict instability failure in circular tunnels and take appropriate preventative measures.
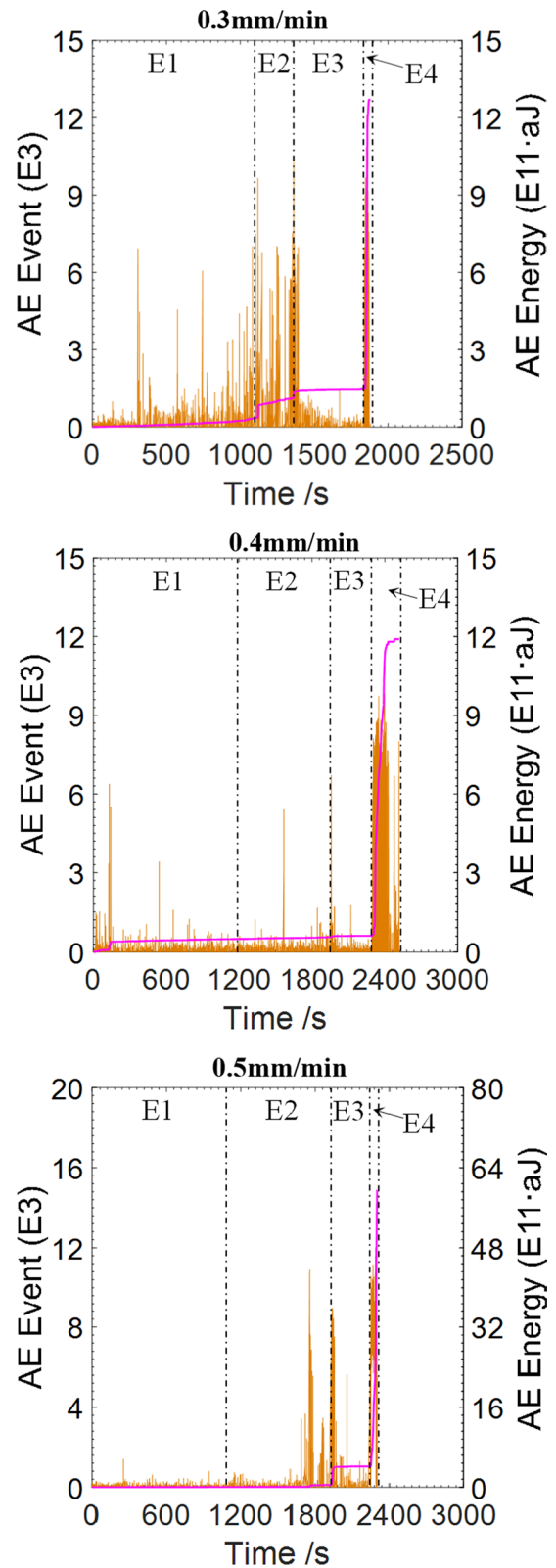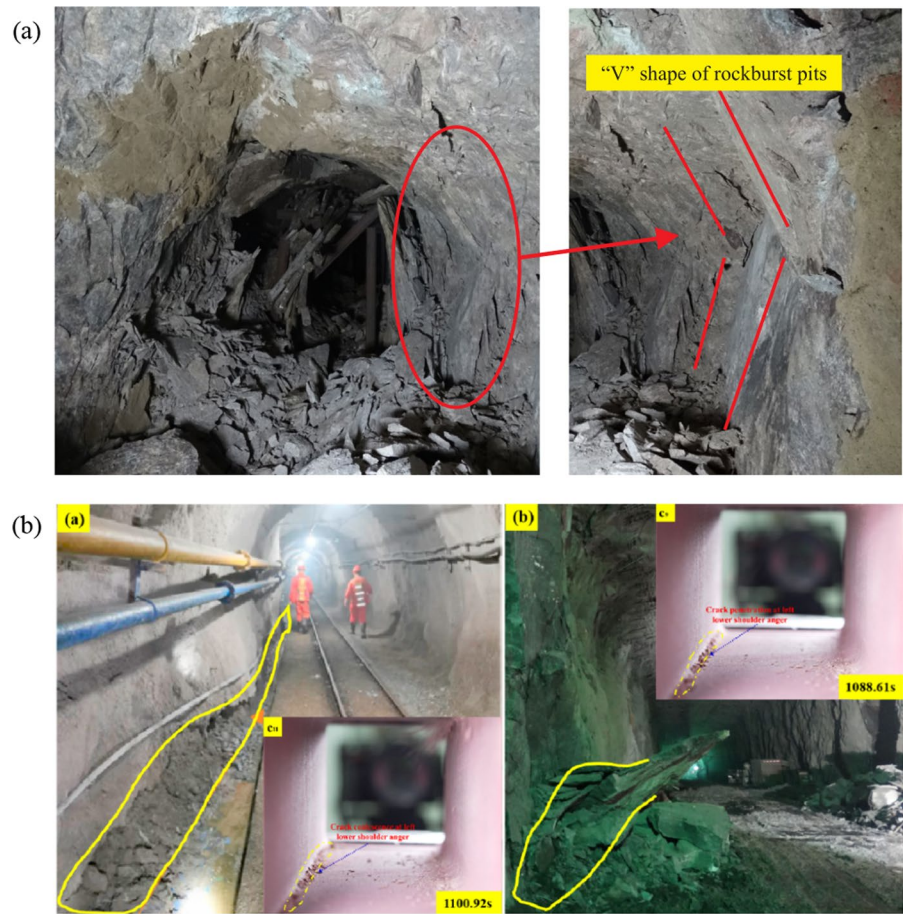
Fig. 11 Tunnel failure at mine *site*. **a** Mine *site* in Erdaogou Gold Mine (Liu et al. 2018); **b** mine *site* in Sanshandao Gold Mine (Jiang et al. 2022)

Author contributions Xun wrote the main manuscript text. Yunming and Kui revised the manuscript text. Xiangxin and Zhengnan prepared figures. All authors reviewed the manuscript.

Availability of data materials The datasets generated and/or analyzed during the current study are available from the corresponding author upon request.

Declarations

Ethics approval and consent to participate Our research in this manuscript does not involve the ethics approval.

Consent for publication The authors declare that they have no known competing financial interests or personal relationships that could have appeared to influence the work reported in this paper.

Competing interest On behalf of all authors, the corresponding author states that there are no competing interests.

Appendix 1

The cumulative strain energy of loading rate 0.3 mm/min on each phase.

| | Strain energy in each phase | | | | Cumulative strain energy | | |
	E1[*]/kJ	E2[**]/kJ	E3[***]/kJ	E4[****]/kJ	(E1+E2) /kJ	(E1+E2+E3) /kJ	(E1+E2+E3+E4)/kJ
GS(0.005)-1	14.68	3.72	5.81	9.19	18.393	24.199	33.392
GS(0.005)-2	14.10	4.45	6.19	3.28	18.552	24.744	28.027
GS(0.005)-3	16.67	3.68	7.01	6.19	20.356	27.368	33.561
GS(0.005)-4	14.09	4.25	8.07	4.89	18.342	26.412	31.298
AVE	14.885	4.026	6.770	5.888	18.911	25.681	31.569

*Strain energy in hydrostatic pressure phase; **Strain energy in particle ejection phase; ***Strain energy in flake stripping phase; ****Strain energy in instability phase.

Appendix 2

The cumulative strain energy of loading rate 0.4 mm/min on each phase.

| | Strain energy in each phase | | | | Cumulative strain energy | | |
	E1/kJ	E2/kJ	E3/kJ	E4/kJ	(E1+E2)/kJ	(E1+E2+E3)/kJ	(E1+E2+E3+E4)/kJ
GS(0.006)-1	13.81	4.10	3.45	9.51	17.910	21.361	30.873
GS(0.006)-2	14.15	5.27	8.23	5.99	19.425	27.659	33.649
GS(0.006)-3	13.84	3.48	6.76	8.29	17.322	24.084	32.378
GS(0.006)-4	14.90	5.00	8.92	4.73	19.895	28.810	33.538
AVE	14.177	4.461	6.840	7.131	18.638	25.478	32.610

*Strain energy in hydrostatic pressure phase; **Strain energy in particle ejection phase; ***Strain energy in flake stripping phase; ****Strain energy in instability phase.

Appendix 3

The cumulative strain energy of loading rate 0.5 mm/min on each phase.

| | Strain energy in each phase | | | | Cumulative strain energy | | |
	E1/kJ	E2/kJ	E3/kJ	E4/kJ	(E1+E2) /kJ	(E1+E2+E3) /kJ	(E1+E2+E3+E4) /kJ
GS(0.008)-1	15.60	5.54	6.08	11.12	21.143	27.224	38.342
GS(0.008)-2	13.55	3.68	8.64	8.06	17.231	25.867	33.923
GS(0.008)-3	14.20	5.69	5.50	12.98	19.888	25.388	38.365
GS(0.008)-4	14.37	3.75	7.26	10.26	18.122	25.379	35.638
AVE	14.428	4.668	6.868	10.602	19.096	25.965	36.567

*Strain energy in hydrostatic pressure phase; **Strain energy in particle ejection phase; ***Strain energy in flake stripping phase; ****Strain energy in instability phase.

References

Chen B, Shen B, Jiang H (2023) Shear behavior of intact granite under thermo-mechanical coupling and three-dimensional morphology of shear-formed fractures. J Rock Mech Geotech Eng 15(3):523–537

Dong L, Chen Y, Sun D et al (2023) Implications for identification of principal stress directions from acoustic emission characteristics of granite under biaxial compression experiments. Int J Min Sci Technol 15(4):789–798

Farhidzadeh A, Mpalaskas AC, Matikas TE et al (2014) Fracture mode identification in cementitious materials using supervised pattern recognition of acoustic emission features. Constr Build Mater 67(2):129–138

Feng X, Gong B, Liang Z, Wang S, Tang C, Li H, Ma T (2024) Study of the dynamic failure characteristics of anisotropic shales under impact Brazilian splitting. Rock Mech Rock Eng 57:2213–2230

Gao L, Gao F, Xing Y et al (2020) An energy preservation index for evaluating the rockburst potential based on energy evolution. Energies 13:1–16

Gong F, Si X, Li X et al (2019) Experimental investigation of strain rockburst in circular caverns under deep three-dimensional high-stress conditions. Rock Mech Rock Eng 52(5):1459–1474

Gong F, Wu W, Ren L (2023) Rockburst process and strength-weakening effect of the high-stress circular tunnel under internal unloading. J Rock Mech Geotech Eng 4:864–885

Hou P, Gao F, Yang YG et al (2016) Effect of the layer orientation on mechanics and energy evolution characteristics of shales under uniaxial loading. Int J Min Sci Technol 26(5):857–862

Huang D, Li YR (2014) Conversion of strain energy in triaxial unloading tests on Marble. Int J Rock Mech Min Sci 66:160–168

Hyun-Ik P, Yeon-Jun et al (2009) A study on the stability of deep tunnels considering brittle failure characteristic. Tunnel Undergr Sp Technol 19(4):304–317

Ishida T, Labuz JF, Manthei G et al (2017) ISRM suggested method for laboratory acoustic emission monitoring. Rock Mech Rock Eng 50(3):665–674

Jiang Q, Xin J, Xu D et al (2022) Shear failure process of rectangular tunnel: physical experimental test and numerical back-analysis. Theoret Appl Fract Mech 120:103384

Jing C, Zhang L (2022) Characterization of tensile crack propagation and energy evolution during the failure of coal-rock samples containing holes. Sustainability 14(21):14279

Lavrov A (2003) The Kaiser effect in rocks: principles and stress estimation techniques. Int J Rock Mech Min Sci 40:151–171

Liang Z, Xue R, Xu N et al (2020) Characterizing rockbursts and analysis on frequency-spectrum evolutionary law of rockburst precursor based on microseismic monitoring. Tunn Undergr Space Technol 105:103564

Liu Z, Zhou C, Yang X (2014) Energy evolution model and critical failure criterion for the dynamic process of tunnel system instability. Geotech Geol Eng 32:1211–1230

Liu X, Liang Z, Zhang Y et al (2018) Experimental study on the monitoring of rockburst in tunnels under dry and saturated conditions using AE and infrared monitoring. Tunn Undergr Space Technol 82(12):517–528

Liu X, Wu L, Zhang Y et al (2019) Frequency properties of acoustic emissions from the dry and saturated rock. Environ Earth Sci 78(3):67

Meng Q, Zhang M, Han L et al (2016) Effects of acoustic emission and energy evolution of rock specimens under the uniaxial cyclic loading and unloading compression. Rock Mech Rock Eng 49(10):3873–3886

Niu S, Ge S, Yang D et al (2018) Mechanical properties and energy mechanism of saturated sandstones. J Central South Univ 25(6):1447–1463

Ohtsu M, Tomoda Y, Suzuki T (2007) Damage evaluation and corrosion detection in concrete by acoustic emission. In: Carpinteri A et al (eds) Fracture mechanics of concrete and concrete structure design. Assessment and retrofitting of RC structures. Taylor and Francis Group, London

Shiotani T (2008) Parameter analysis. In: Grosse C, Ohtsu M (eds) Acoustic emission testing. Springer, Berlin, pp 41–51

Si X, Li X, Gong F et al (2022) Experimental investigation of failure process and characteristics in circular tunnels under different stress states and internal unloading conditions. Int J Rock Mech Min Sci 154:105116

Smittarello D, Smets B, Barrière J et al (2022) Precursor-free eruption triggered by edifice rupture at Nyiragongo volcano. Nature 609:83–88

Wang CL, Du GY, Han Y et al (2023) Evolution characteristics of acoustic emission and strain energy for deep granite under different damage stages. Geomech Geophys Geo-Energy Geo-Resour 9(1):14

Xie H, Ju Y, Li L et al (2008) Energy mechanism of deformation and failure of rock masses. Chin J Rock Mech Eng 27(9):1729–1741

Xue R, Liang Z, Xu N et al (2020) Rockburst prediction and stability analysis of the access tunnel in the main powerhouse of a hydropower station based on microseismic monitoring. Int J Rock Mech Min Sci 126:104174

Yin X, Li S, Tang H et al (2009) Study on quiet period and its fractal characteristics of rock failure acoustic emission. Chin J Rock Mech Eng 28(Sup2):3383–3390

Zhai M, Xue L, Bu F et al (2022) Effects of bedding planes on progressive failure of shales under uniaxial compression: insights from acoustic emission characteristics. Theoret Appl Fract Mech 119:103343

Zhang Y, Feng X, Yang C et al (2019a) Fracturing evolution analysis of Beishan granite under true triaxial compression based on acoustic emission and strain energy. Int J Rock Mech Min Sci 117:150–161

Zhang Y, Feng X, Zhang X et al (2019b) Strain energy evolution characteristics and mechanisms of hard rocks under true triaxial compression. Eng Geol 260:1–14

Zhang Y, Feng X, Zhang X et al (2019c) A novel application of strain energy for fracturing process analysis of hard rock under true triaxial compression. Rock Mech Rock Eng 52(11):4257–4272

Zhang R, Liu Y, Hou S (2023) Evaluation of rockburst risk in deep tunnels considering structural planes based on energy dissipation rate criterion and numerical simulation. Tunn Undergr Space Technol 137:105128

Zhao K, Yang D, Zeng P et al (2021a) Effect of water content on the failure pattern and acoustic emission characteristics of red sandstone. Int J Rock Mech Min Sci 142:104709

Zhao Z, Sun W, Chen S et al (2021b) Determination of critical criterion of tensile-shear failure in Brazilian disc based on theoretical analysis and meso-macro numerical simulation. Comput Geotech 134:104096

Zhao Z, Liu H, Gao X et al (2023) Meso-macro damage deterioration of weakly cemented red sandstone under the coupling effect of high-humidity and uniaxial loading. Eng Fail Anal 143:106911

Zhao J, Duan S, Chen B et al (2024) Failure mechanism of rock masses with complex geological conditions in a large underground cavern: a case study. Soil Dyn Earthq Eng 177:108439

Publisher's Note Springer Nature remains neutral with regard to jurisdictional claims in published maps and institutional affiliations.